Biomaterials Science

ROYAL SOCIETY OF CHEMISTRY

PAPER

View Article Online
View Journal | View Issue

Cite this: *Biomater. Sci.*, 2025, **13**, 5522

Wound-healing biodegradable microparticles: an *in vitro* investigation

Zeynep Imir Tekneci,[a] Akmal Bin Sabri,[a] Adam A. Dundas,[b] Derek J. Irvine,[c] Amir M. Ghaemmaghami[d] and Morgan R. Alexander *[a]

Received 12th June 2025,
Accepted 3rd August 2025

DOI: 10.1039/d5bm00896d

rsc.li/biomaterials-science

Wound healing is a complex process that may result in healthy tissue regeneration, but problematic chronic wounds exhibit fibrosis and persistent inflammation. To improve wound outcomes, the application of pro-proliferative polymers as bioresorbable particles was investigated for the first time. The surface of bioresorbable poly(D,L-lactic acid) ($P_{DL}LA$) microparticles is decorated with a pro- and anti-proliferative polymer that adheres to the surface for a minimum of 21 days. Microparticles with a pro-proliferative polymer surface chemistry have been shown to increase fibroblast proliferation *in vitro* by 5 fold after 48 hours compared to cells without microparticle treatment. The cells are found to move to establish bridges between the microparticles, which facilitate cell elongation and proliferation, accelerating a key stage of the wound healing cycle. Adsorbed proteins were examined using proteomics, and unique proteins were found to adhere to microparticles exhibiting proliferative surface chemistry. These proteins include annexin, olfactomedin 4 and vimentin, and the roles of these proteins have been highlighted to gain a mechanistic insight into the stimulated proliferative environment caused by the microparticles. The lipid deposition/retention from exposure to the culture media of microparticles was investigated using 3D Orbi-SIMS and highlights preferential adsorption of lipids, including sterols, fatty acids and sphingolipids, which correlates with pro- and anti-healing polymers. This mechanistic insight helps advance this technology to address the pressing issue of chronic wound healing.

1. Introduction

Wound healing is a multifaceted process that involves the coordinated activity of several types of cells, occurring in four consecutive phases: haemostasis, inflammation, proliferation and migration, and tissue remodelling.[1] Haemostasis is the initial stage of wound healing, involving scab formation to seal the wound and releasing chemotactic factors that stimulate inflammatory cells. In the inflammatory phase, immune cells secrete cytokines to induce proliferation and sanitize the wound area by phagocytosing microbes and cell debris. The granulation tissue is generated during the proliferation and migration of myoblasts, endothelial cells and fibroblasts and is replaced by normal connective tissue in the final phase, remodelling. The wound healing process may result in fibrosis, scar tissue formation, or regeneration, depending on the components of the cellular environment controlled by secreted cytokines, chemokines, and growth factors by macrophages and fibroblasts. The ability of fibroblasts to regulate the extracellular matrix (ECM) makes them a key player in wound healing.[2–4]

In chronic wounds, such as diabetic wounds, the healing process is disrupted due to persistent inflammation limiting the progression to the proliferation phase.[5] The proliferation and migration of fibroblasts within the chronic wound ECM decrease, coupled with the dysregulation of cytokine secretion, which contributes to delayed healing and persistent inflammation.[6,7] Chronic wounds affect millions worldwide, especially diabetics for whom the incidence of lower limb amputations results in very high mortality rates.[8] Patients with diabetic foot ulcers who undergo amputation face elevated mortality rates of 13 to 40% within the first-year post-operation, escalating to 39–80% by the fifth year.[9] There are opportunities to improve care using innovative active dressings to alleviate the substantial costs and suffering experienced by those affected. Bio-instructive materials have shown promise in accelerating wound healing without the use of soluble active pharmaceutical ingredients, thus offering a new treatment modality.

When a biomaterial comes into contact with the body, a distinct biological identity is formed through the adsorption of proteins. These proteins on the bio-interface determine

[a]*School of Pharmacy, University of Nottingham, Nottingham NG7 2RD, UK. E-mail: morgan.alexander@nottingham.ac.uk*
[b]*Advanced Materials Research Group, Faculty of Engineering, University of Nottingham, Nottingham NG7 2RD, UK*
[c]*Centre for Additive Manufacturing, Faculty of Engineering, University of Nottingham, Nottingham, NG7 2RD, UK*
[d]*School of Life Sciences, University of Nottingham, Nottingham NG7 2RD, UK*

innate immune cell reactions.[10,11] In addition to surface-adsorbed proteins, lipid deposition/retention on biomaterials has recently been shown to play an important function in cell–biomaterial interactions because of their role in inflammation and fibrosis.[12] Schreib *et al.* investigated lipid deposition on the surface of a biomaterial post-implantation using time-of-flight secondary ion mass spectrometry (ToF-SIMS).[13] They observed high fatty acid deposition on implants with pro-inflammatory characteristics, which promotes the transcription of pro-inflammatory genes. The advancement of a high-resolution Orbitrap mass analyzer in 3D Orbi-SIMS has further improved the specificity of ion assignments.[14] Suvannapruk *et al.* employed 3D Orbi-SIMS to identify metabolites in the tissue surrounding catheters that were coated with pro-inflammatory and anti-inflammatory polymers. They reported significantly higher glycerolipid deposition in the surrounding tissue implanted with a pro-inflammatory polymer coating.[15] Physicochemical properties of biomaterials influence the adsorption process[16] and therefore by altering the physicochemical characteristics of biomaterials, cell behavior, including cell attachment, proliferation, differentiation, and migration, can be modulated.[17–19] Besides chemical composition, surface charge, size, and the shape of biomaterials, researchers have recently elucidated that stereochemistry is also responsible for adsorption mechanisms at the bio-interface and cell responses.[20] For example, Hu *et al.* reported that D-chiral PLA membranes suppress inflammation and facilitate re-epithelialization.[21] Over the past ten years, high-throughput (HT) technologies have revolutionized biomaterials discovery by enabling the creation of customized materials for many purposes, such as preventing biofilm formation and modulating monocyte differentiation.[22–26]

Biocompatibility and biodegradability are desirable factors in selecting biomaterials to ensure that successful treatment is achieved without causing any accumulation of and/or adverse reactions to polymer byproducts in the body, either during or post-treatment. Polylactic acid (PLA) and polylactic-*co*-glycolic acid (PLGA) are among the most common biodegradable polymers utilized in various biomedical applications, due to the fact that their biocompatibility and biodegradability have been well-established.[27–32] Moreover, they are suitable materials from which microparticles can be produced because of their compatibility with a wide range of additives. For instance, utilizing bio-instructive polymeric surfactants and $P_{DL}LA$ as a core material for the microfluidic production of microparticles results in uniform particle size and the desired surface chemistry.[33]

In previously published work, fibroblast instructive surface chemistries were identified as either pro- or anti-proliferative and then transformed into bio-instructive surfactants.[25,34] In this initial study, non-bioresorbable microparticles were fabricated by utilizing a fibroblast-instructive surfactant to deliver both the desired surface chemistries and droplet stability. Pro-proliferative microparticles were then successfully utilized in a

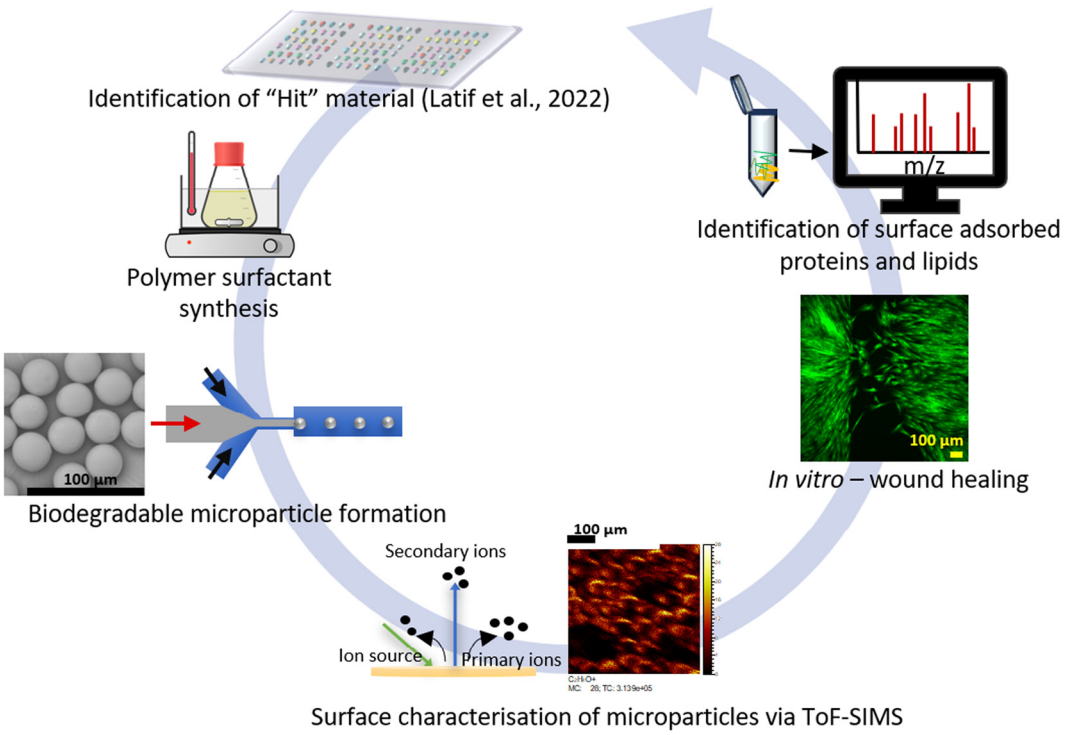

Fig. 1 Schematic illustration of the discovery of "Hit" materials to accelerate wound healing. The materials identified *via* polymer microarrays are the main components of the synthesized surfactants. The surfactants were used in a flow-focusing microfluidic chip to produce surface-functionalized biodegradable microparticles. After confirming surface functionality using time of flight-secondary ion mass spectrometry (ToF-SIMS), the particles were incubated with skin fibroblast cells to evaluate the impact of the microparticle surface on cell proliferation and wound healing.

wound on a diabetic mouse model and they successfully accelerated the healing over a 20-day period.[25]

In this paper, we search for mechanistic insights into the healing process promoted by these particles by characterizing the bio-interface between cell-instructive microparticles and skin fibroblast cells in an *in vitro* wound healing model (Fig. 1). Furthermore, a biodegradable polymer core with bio-instructive surfactants was used to fabricate functional microparticles, for controlling cells. In an *in vitro* wound healing model, the introduction of biodegradable particles with a pro-proliferative surface chemistry led to an increase in fibroblast proliferation. In addition, it was discovered that fibroblasts formed cellular bridges between the microparticles, which demonstrate cell elongation *in vitro*. Uniquely adsorbed proteins and lipid deposition on each microparticle type were identified to elucidate the possible biomaterial surface–cell interaction mechanism that orchestrates the wound healing process.

2. Results and discussion

2.1. Microparticle production and characterization

Poly(D,L-lactic acid) ($P_{DL}LA$) was selected as a biodegradable core material for use in this study. The amorphous structure of $P_{DL}LA$ demonstrates high mechanical stability, biocompatibility and accelerated degradation.[21,35] Monodisperse particle sizes were obtained by generating microparticles using a droplet microfluidic method successfully as described in a previously published study.[33] The recently identified polymeric surfactants with anti-proliferative and pro-proliferative bio-stimulatory functionalities present in the dispersed phase feed provided both stable emulsion formation and the desired proliferation-promoting surface chemistry.[25] The surfactants were synthesized by co-polymerizing cell-instructive monomers with a hydrophilic co-monomer *via* a technique called catalytic chain transfer polymerization. The macromer poly(ethylene glycol) methyl ether methacrylate ($mPEGMA_{300}$) was chosen as a hydrophilic co-monomer because it can be obtained in several variants with different molecular weights and end groups. In practice, $mPEGMA_{300}$ was found to provide higher conversion during surfactant synthesis, so it was the primary variant used in this study. It was then used in a desired target copolymer ratio of 90 : 10 (bio-stimulatory monomer : $mPEGMA_{300}$) to successfully produce stable emulsion droplets.[36] The conversions were 84 and 60% for the copolymerization of $mPEGMA_{300}$ with ethylene glycol phenyl ether acrylate (EGPEA) and tetrahydrofurfuryl acrylate (THFuA) monomers, respectively (Fig. S1, SI). The molecular weights of the polymeric surfactants, EGPEA-*co*-$mPEGMA_{300}$ (anti-proliferative) and THFuA-*co*-$mPEGMA_{300}$ (pro-proliferative), were 14.9 and 19.7 kDa, respectively (Fig. S2, SI).[23] These molecular weights were found to be within the limits of the operating parameters of the microfluidic system (15–25 kDa), to ensure an optimal viscosity for the dispersed phase.

The dispersed phase containing $P_{DL}LA$ (of concentration 5% (w/v)) in ethyl acetate and 0.1% (w/v) of cell-instructive surfactant was introduced into the microfluidic system while 0.1% (w/v) polyvinyl-*co*-acetate (PVA) in water solution was used as the continuous phase. In the production of microparticles without using cell-instructive surfactant in the dispersed phase, 2% (w/v) PVA in water solution was used as a continuous phase to ensure stable emulsion formation. When the dispersed phase core material content was prepared using commercial $P_{DL}LA$ (M_n 47 000 g mol^{-1}), there was repeated blockage in the microfluidic system due to high solution viscosity. To overcome this problem, a low molecular weight $P_{DL}LA$ (M_n 2209 g mol^{-1}) was synthesized as described in previously published work[37] and the dispersed phase was prepared using 25% low molecular weight $P_{DL}LA$ and 75% commercial $P_{DL}LA$.

To characterize the form and surface of the microparticles, scanning electron microscopy (SEM) and time of flight-secondary ion mass spectrometry (ToF-SIMS) were utilized, respectively, with the results obtained being shown in Fig. 2. The SEM images demonstrate that the particle sizes obtained with EGPEA-*co*-$mPEGMA_{300}$ and THFuA-*co*-$mPEGMA_{300}$ and without a bio-functional surfactant in the dispersed phase are 26.2 ± 1.5 μm, 28.9 ± 1.2 μm and 20.8 ± 1.2 μm, respectively. The particles produced without a bio-functional surfactant had a slightly smaller size, which could be due to the high surfactant concentration (2% w/v PVA) in the continuous phase. Also, PVA performs as a better surfactant causing tighter particle formation. All particles produced with or without cell-instructive surfactants had a coefficient of variation close to 5%, indicating a monodisperse particle size distribution.

The surface chemistry of microparticles was confirmed by analyzing both positive and negative spectra and ion maps acquired from ToF-SIMS. Unique ions located on the surface of EGPEA-*co*-$mPEGMA_{300}$ and THFuA-*co*-$mPEGMA_{300}$ microparticles were identified as $C_6H_5O^-$ and $C_5H_9O^+$, respectively. As shown in Fig. 2d, both surfactants were localized successfully indicating that cell-instructive chemistries decorated the particle surfaces as desired. Microparticles fabricated using commercial surfactant show lower $C_6H_5O^-$ and $C_5H_9O^+$ ion intensities, while the $C_4H_9O^+$ ion, which is unique for the PVA surfactant, is located on the surface. Although this commercial surfactant is used in the continuous phase when producing particles with EGPEA-*co*-$mPEGMA_{300}$ and THFuA-*co*-$mPEGMA_{300}$, the surface chemistry is dominated by cell-instructive surfactants introduced in the dispersed phase.

The degradation of microparticles was investigated by calculating weight loss percentages in cell culture medium with different protein concentrations. Minimum essential medium (MEM) with 0%, 3%, 6% and 10% (v/v) protein concentrations was prepared using foetal bovine serum (FBS) in required amounts. After immersing the particles for 2 weeks in MEM only, without any proteins, the weight loss of the particles with anti-proliferative, pro-proliferative and commercial surfactants was 35%, 31%, and 60%, respectively (Fig. 2g). When protein was introduced into the media, the weight loss decreased, indi-

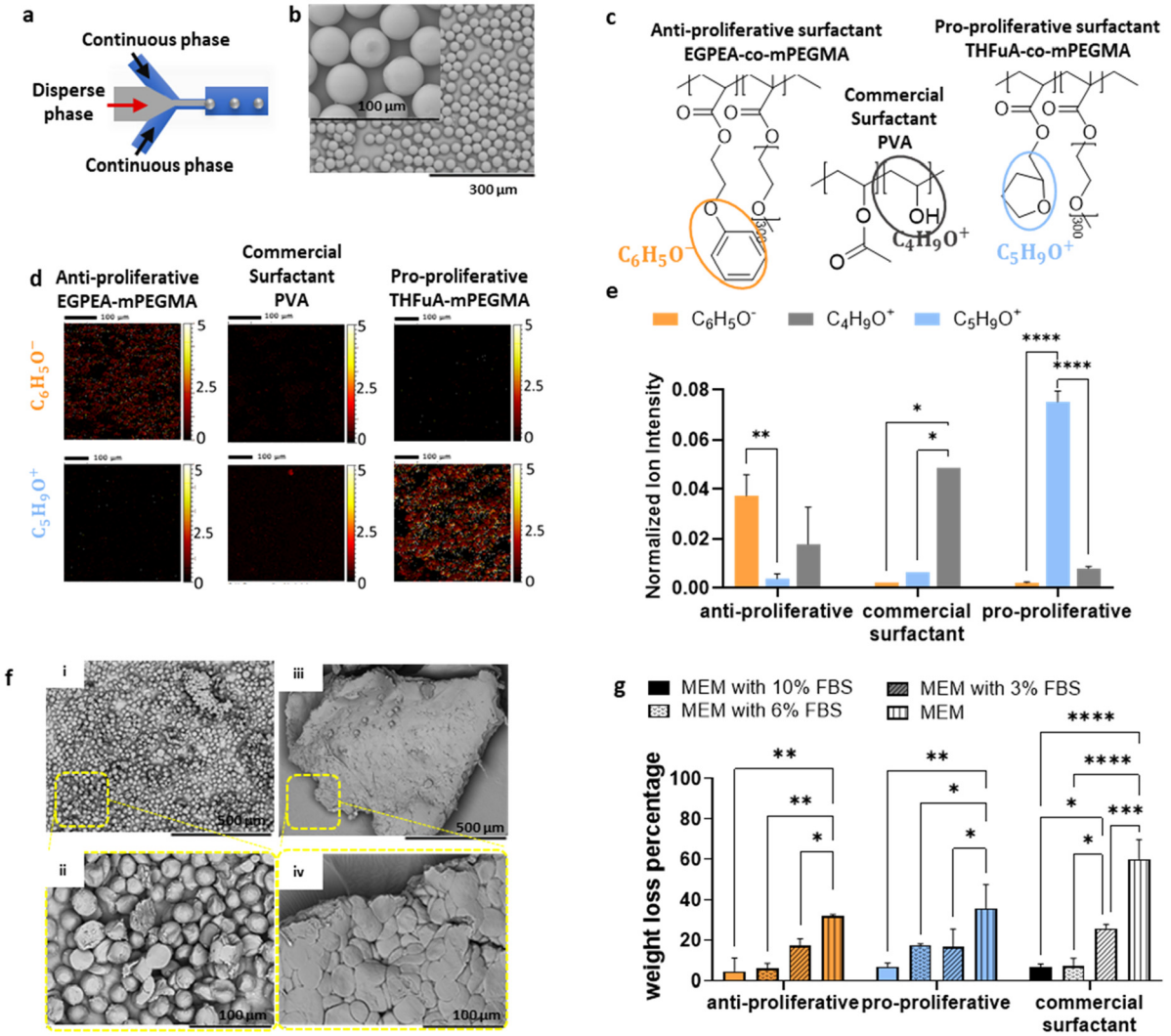

Fig. 2 (a) Schematic of a microfluidic chip with flow-focusing geometry. (b) SEM images of pro-proliferative particles produced with a THFuA-mPEGMA surfactant with a size of 28.9 ± 1.2 µm (COV = 4.3%) n = 100, scale bars are 300 µm and 100 µm. (c) Chemical structures of surfactants. (d) ToF-SIMS data showing the identification of unique ions for EGPEA ($C_6H_5O^-$) and THFuA ($C_5H_9O^+$) on polymer microparticles. Chemical image maps of unique ions for each particle are shown. N = 3 regions of interest used, scale bar = 100 µm. (e) Normalized ion intensities of each unique ion for particles with three different surface chemistries are shown in the graph. (f) SEM images of pro-proliferative particles incubated in MEM without protein (MEM only) at ×150 (i) and ×600 (ii) magnifications and with protein (MEM with 10% FBS) at ×150 (iii) and ×600 (iv) magnifications for 40 days. (g) Weight loss percentages of biodegradable particles in media in 13 days with different serum protein concentrations. *p < 0.1, **p < 0.01, ***p < 0.001, ****p < 0.0001.

cating the retardation of degradation due to protein dissolution (Fig. 2f). This is likely explained by the protein layer acting as a barrier to water penetration into the surface of microparticles.

The lifespan of biodegradable biomaterials is a critical parameter in ensuring that the material remains in place for sufficient time to elicit its wound healing effect during the treatment duration. Following an injury, it has been shown that fibroblasts migrate to the wound area within 5–7 days and wound healing is usually completed within 5–10 days in the case of acute wounds.[3,38] However, wounds defined as chronic require months or years to heal in most cases.[39] In the current work, it has been shown that both anti- and pro-proliferative particles lost less than 10% of their initial weights at the end of day 13 in MEM with 10% FBS. Particles were clumped together after 40 days of incubation in cell culture media with 10% FBS, and no decomposition was observed (Fig. 2f). In the literature, generally, media with at least 20% serum concentration have been utilized to mimic wound-like environments.[40,41] The higher protein concentration in wound environments slow down degradation further. Moreover, it has been confirmed that bio-functional surfactants remain on the surface of microparticles after 21 days of incubation at 37 °C in DI water, which is a harsh environment to degrade particles and the required time period for complete healing.[42] This indicates that biodegradable particles can maintain their efficiency

for at least 21 days and continue to function for longer healing periods, which is required for chronic wounds.

Due to the biodegradable nature of PLA, these microparticles ultimately undergo degradation. For example, Visscher *et al.* studied the *in vivo* degradation of PLA microcapsules, and they observed the first breakdown after 150 days and complete erosion after 420 days.[43] This timeframe is expected to surpass the healing duration of many wounds. Considering the pro-healing properties of surfactants and the high biocompatibility of PLA, negative biological effects are not anticipated. However, the degradation rate of PLA can be adjusted by modifying its molecular weight to accelerate degradation.

2.2. *In vitro* wound healing assay

To test for toxicity, cell viability on microparticles was assessed. The fibroblasts cultured on each of the microparticles had high levels of viability (Fig. S4, SI). In this study, microparticles travelled through the collection vessel containing water to ensure the complete removal of ethyl acetate from $P_{DL}LA$ droplets within the water phase during microfluidic production. Therefore, the risk of toxic solvent residue diffusing from the particles into the culture medium is minimized, and viability data showed that all microparticles promoted high cell viability.

Fibroblasts were seeded on microparticles and studied *via* live imaging for 72 h. The movement of single cells was examined using live imaging with three-minute intervals. Cells were located on the tissue culture plate and adhered to the bottom surface of particles. This dynamic movement starts with the attachment of cells to the particles. As cells migrate and form bridges, particles are swept along by cells (see the SI video: fibroblast cultured on THFuA-mPEGMA core PLA). It was observed that fibroblasts incubated with pro-proliferative microparticles exhibited tumbling-like cell movements before they elongated and attached to any particles.

Recently, Ayushman *et al.* reported that minute-scale tumbling motions of cells in the early incubation stage modulate the differentiation of stem cells.[44] The fibroblasts cultured on the microparticles attached and became elongated following 12 hours of incubation. Following cell elongation, cell bridges, characterized by dynamic connections between fibroblasts and microparticles, were formed (Fig. S5). The position and number of these cell bridges were continuously changing depending on cell migration and proliferation. Cell-to-cell communication, the fundamental mechanism underlying all biological processes, is mediated *via* both cytoplasmic connections and non-cytoplasmic connections. Cytoplasmic connections, such as gap junctions, link cells together to build interconnected supracellular assemblies.[45] These cell bridges not only enable cell-to-cell communication by transferring the signaling component but also permit crosstalk between the cell and biomaterial interface. Cell bridges are established during the initial stage of cellular differentiation and offer convincing evidence of the compatibility between cells and biomaterials.[46–49]

The wound closure performance of anti- and pro-proliferative microparticles was studied by performing an *in vitro* wound healing assay. The fibroblast proliferation and cytokine content of the wound microenvironment were also investigated to offer some mechanistic insights into the observed differences.

The wound area treated with pro-proliferative microparticles exhibited higher closure than that treated with anti-proliferative microparticles and the TCP control without particles after 12 h, 24 h and 48 h. By 72 hours, the area of injury treated with pro-proliferative microparticles and TCP control had closed by a similar amount (Fig. 3a and b), $p > 0.1$. This is likely due to contact inhibition of proliferation (CIP), an important characteristic of non-cancerous cells resulting in the inhibition of proliferation and cell division when all space is covered due to high cell density, meaning cells are confluent.[50] Wound closure percentages observed in the area treated with anti-proliferative microparticles were the lowest at all time points.

The effect of the microparticles on proliferation during *in vitro* wound healing was investigated *via* Ki-67 antibody expression at 48, 72 and 96 h post-wounding. Ki-67 is commonly used as a proliferation marker due to its presence in the interphase and mitosis phase of cell cycles while it is dramatically downregulated in resting (G0 phase) cells.[51] Pro-proliferative particles conferred significantly higher Ki-67 antibody expression, especially at 48 h, compared to TCP and anti-proliferative particles (Fig. 4a). The decrease in Ki-67 antibody expression of cells treated with pro-proliferative particles at 72 h and 96 h may be explained *via* CIP. Due to accelerated cell migration and proliferation in the first 48 hours, fibroblasts occupied the available space, and this led to a slowdown in proliferation. Wound healing was accelerated in the early stages and proliferation slowed down at 96 hours. This indicates that proliferative microparticles could not stimulate fibrotic responses, which is undesirable for healthy, scarless healing.

Cell behavior and phenotype, which are the key factors in determining the fate of healing, mainly depend on the secreted cytokines and growth factors within the cellular milieu. To investigate the effect of microparticles on the cell microenvironment, secreted growth factors and cytokines in the wound healing environment were assessed by evaluating concentrations of basic fibroblast growth factor (bFGF), hepatocyte growth factor (HGF), monocyte chemoattractant protein-1 (MCP-1) and interleukin 6 (IL-6). Both HGF and bFGF concentrations in the wound treated with pro-proliferative particles were significantly higher than in wounds treated with anti-proliferative microparticles (Fig. 4d and e). Fibroblasts and monocytes are the primary cell types driving the wound healing process due to their ability to control proliferation and inflammation. Therefore, fibroblast-derived monocyte stimulatory cytokines, namely MCP-1 and IL-6, were examined to gain an understating of the potential impact of fibroblasts' secretome on the behavior of monocytes and macrophages. MCP-1 functions as a chemokine to regulate

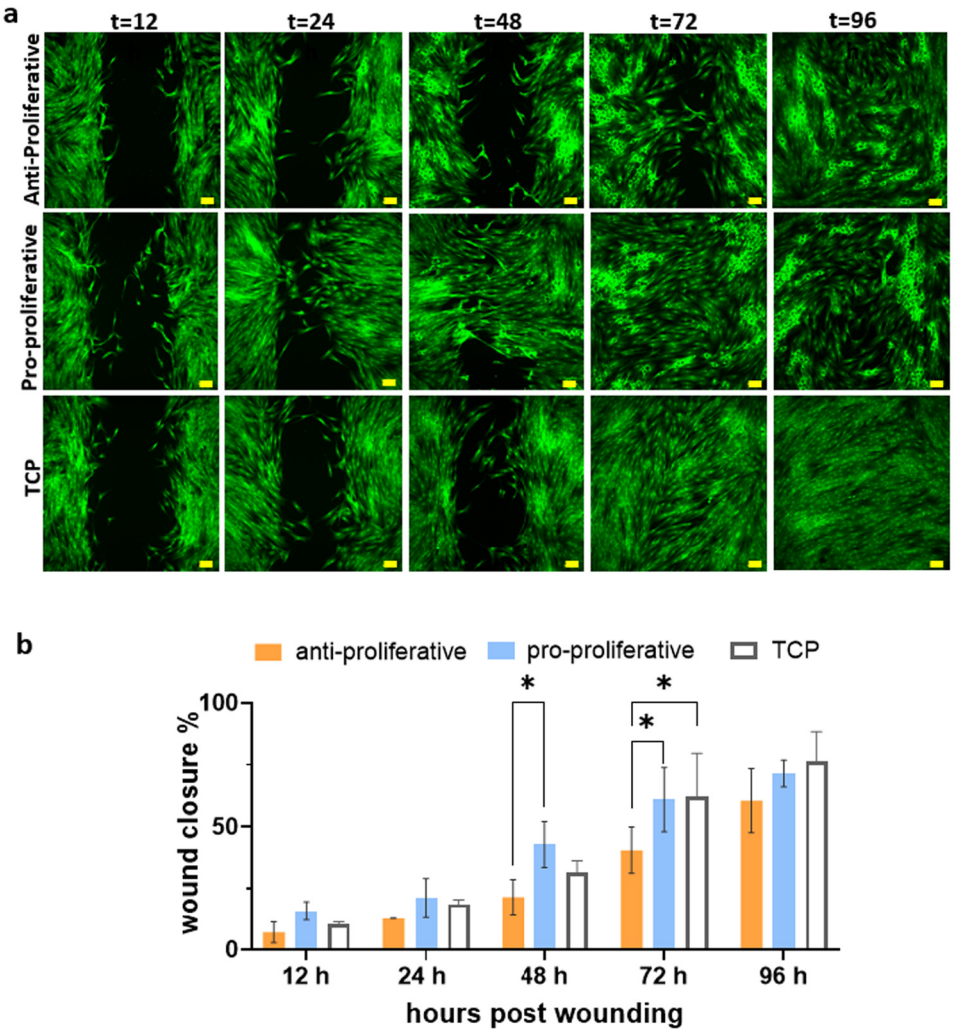

Fig. 3 *In vitro* wound healing assay was employed by treating wound gaps with anti-proliferative and pro-proliferative core $P_{DL}LA$ microparticles. Wound gaps were created on TCP. (a) Microscopy images show fibroblast growth and wound area closure at 12 h, 24 h, 48 h, 72 h and 96 hours post-wounding. Scale bar = 100 μm. (b) Wound closure percentages of wounds treated with antiproliferative microparticles (orange bars), with pro-proliferative microparticles (blue bars) and without any microparticles (white bars = TCP) $N = 3$, $n = 4$. *$p < 0.1$.

monocyte migration, and IL-6 induces upregulation of functional M-CSF receptor on monocytes allowing them to use their autocrine M-CSF, hence supporting their differentiation into macrophages[52,53]Although there is no significant difference, the wound treated with anti-proliferative particles exhibited higher concentrations of IL-6 and MCP-1, which are known to be a pro-inflammatory cytokine and a chemoattractant for monocytes, respectively (Fig. 4b and c). These cytokines might potentially stimulate the migration of macrophages into the wound area thereby exacerbating inflammation. It is known that bFGF enhances wound healing and tissue repair by stimulating proliferation.[54] HGF enhances healing in both acute and chronic wounds due to its stimulatory effect on angiogenesis, the growth of fibroblasts, and epithelialization.[55,56] Synchronized secretion of the growth factors bFGF, promoting proliferation, and HGF modulating the cell response to the pro-fibrotic cytokine TGF-β1, enables accelerated healing without fibrosis thus obviating the formation of scar tissue.[57]

2.3. Identification of uniquely adsorbed protein on cell-instructive microparticles

Surface-adsorbed proteins on both anti- and pro-proliferative microparticles were investigated to understand the underlying mechanism of the biomaterial–cell interactions during the wound healing process. This was undertaken without the cells, to understand which proteins preferentially adsorb to the surfaces from the media to initiate the cell response. Microparticles were incubated in the cell culture MEM with 10% FBS overnight without cells. The medium has a concentration of 3–4.5 mg mL^{-1} total protein, including 33.83 μM albumin and 1.3 μM alpha-1-acid glycoprotein.[58] After gently rinsing in PBS and ultrapure water to remove loosely attached molecules, the species remaining adsorbed to the surface were extracted from the surface using concentrated urea solution. These strongly adsorbed proteins were separated on a gel for subsequent protein identification from the

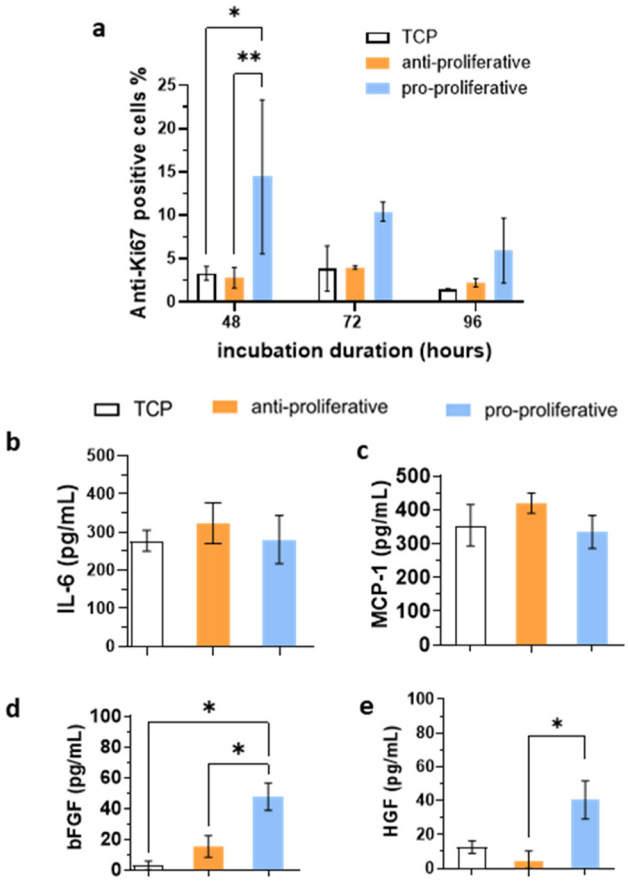

Fig. 4 (a) Fibroblast proliferation detected *via* Ki-67 antibodies, $N = 2$, $n = 3 \pm$ SD. (b) IL-6, (c) MCP-1 cytokines and (d) bFGF and (e) HGF growth factors secreted during *in vitro* wound healing ($N = 2$, $n = 3 \pm 1$SD). *$p < 0.1$, **$p < 0.01$.

bands using liquid chromatography mass spectrometry-mass spectrometry (LC-MS/MS), following previously reported procedures.[23,59]

In all, 189 uniquely adsorbed proteins were identified on the THFuA-*co*-mPEGMA$_{300}$ (pro-proliferative) microparticles, while 125 uniquely adsorbed proteins were found on the EGPEA-*co*-mPEGMA$_{300}$ (anti-proliferative) microparticles. The pro- and anti-proliferative microparticle surfaces shared the adsorption of 175 proteins (Fig. 5). Table 1 presents the top 10 most abundant proteins that were uniquely adsorbed on either anti- or pro-proliferative microparticles. The abundance values have been assessed by the exponentially modified protein abundance index (emPAI), and proteins are listed in decreasing order of abundance.[60] Literature searches reveal that vimentin and heat shock protein β1, proteins in the top 10 highly adsorbed on pro-proliferative microparticles, have a substantial impact on fibroblast proliferation and wound healing.[61–64] Furthermore, surfaces treated with these proteins influence the behavior of cells. For example, Bucki *et al.* revealed that fibroblasts attached to a vimentin-coated surface exhibit a different morphology compared to cells attached to the same substrate with collagen coating.[65] Hammad *et al.* observed that pretreatment of the surface with a combination of human heat shock protein 1-like and human heat shock protein-90 enhanced the attachment of pluripotent cells on polymers.[59]

Searching the literature, seven proteins (*i.e.* annexin, ceruloplasmin, complement 3, heat shock protein β1, small proline-rich 3, olfactomedin 4, and vimentin), out of a total of 189 uniquely adsorbed proteins, have essential functions in fibroblast proliferation and wound healing either in soluble form or intercellularly, as shown in Table 2. The function of these proteins at the interface with cells may not necessarily match their impact on cell proliferation or wound healing in soluble form or intracellularly. Nevertheless, it is reasonable to hypothesize that differential adsorption of these biomolecules on pro- and anti-proliferative polymers contributes to the bio-instructive effects observed here. Moreover, besides working individually, the combinatorial mixtures of ECM proteins may affect cell behavior. Flaim *et al.* studied the synergistic effect of col-

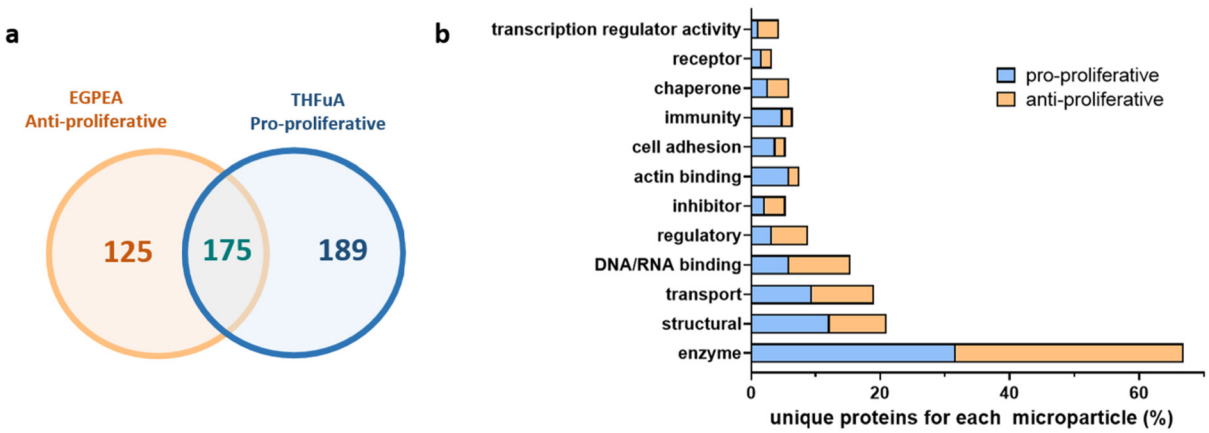

Fig. 5 Proteins uniquely adsorbed to each surface. (a) Venn diagram shows the number of adsorbed proteins identified by LC-MS/MS analysis on microparticles with 2 different surface chemistries (upon overnight incubation with MEM supplemented with 10% FBS, 1% L-glutamine, 1% penicillin and streptomycin, 1% MEM non-essential amino acid solution, and 1% sodium pyruvate solution). (b) A bar graph classifying proteins by their function, with proteins uniquely adsorbed on pro-proliferative (blue bars) and anti-proliferative (orange bars) microparticles.

Table 1 The 10 most abundant unique proteins adsorbed by anti-proliferative and pro-proliferative particles

Anti-proliferative		Pro-proliferative	
Protein name	Abundance (emPAI)	Protein name	Abundance (emPAI)
Histone H2B type 1-N	19.94	Vimentin	2.17
Histone H2A type 1	4.28	Ras-related protein Rab-11A	1.63
Dual specificity protein phosphatase 14	3.38	Coactosin-like protein	1.4
Histone H2A	2.75	Myosin light polypeptide 6	1.3
Proteasome subunit alpha type	1.98	ATP synthase subunit epsilon, mitochondrial	1.16
Proteasome subunit alpha type-7	1.77	Actin-related protein 2/3 complex subunit 4	0.97
Tubulin alpha-1B chain	1.56	14-3-3 protein beta/alpha	0.96
Proteasome subunit beta type-1	1.45	14-3-3 protein gamma	0.95
Actin, aortic smooth muscle	1.41	Heat shock protein beta-1	0.88
Proteasome subunit beta type-3	1.25	Protein S100	0.86

Table 2 Contributions of some uniquely adsorbed proteins on pro-proliferative particles in the healing process

Unique proteins adsorbed on THFuA microparticles	Role in wound healing	Ref.
Annexin	Functions in soluble form: injection of nanoparticles loaded with an annexin mimetic peptide accelerated colonic wound healing in mice.	67
Ceruloplasmin	Ceruloplasmin acts as an antioxidant and prevents secondary tissue degeneration in spinal cord contusion injuries by oxidizing toxic ferrous iron.	68
Complement C3	Functions in soluble form: topical application of complement C3 promotes wound healing in rats by increasing collagen I and fibronectin.	69
Heat shock protein B1	Intracellular function: HspB1-deficient mice showed increased inflammation, reduced proliferation and re-epithelialization.	61
Small proline-rich 3	SPR3 serves as a flexible cross-bridging protein, enhancing the tensile strength of epidermis cells.	70
Olfactomedin 4	Functions in soluble form: Keratinocyte proliferation and migration fibroblast migration were stimulated *via* olfactomedin 4. The topical application of this protein promoted wound healing *in vivo*.	71
Vimentin	Vimentin plays a vital role in wound healing by contributing to all stages of healing and giving structural support to cells and tissues during tissue restoration. Its deficiency hinders wound healing, affecting immune cell migration, fibroblast functions, transforming growth factor-β signalling, and epithelial-to-mesenchymal transition.	62
	Intracellular function: exosomal vimentin promotes fibroblast migration, proliferation, and ECM secretion. *In vitro* and *in vivo*, exosomal vimentin accelerates healing and minimizes scarring.	63
	Intracellular function: the fibroblasts of vimentin-deficient mice exhibit delayed migration, resulting in delayed healing.	64

lagen I, collagen III, collagen IV, laminin, and fibronectin in 32 different combinations on embryonic stem cell differentiation to hepatocyte using a microarray platform. They revealed that the cells exhibited the highest hepatic activity in the ECM combination of laminin, collagen I, and fibronectin.[66] Exploring the role of the differentially adsorbed biomolecule in fibroblast differentiation and wound healing will be a subject of future studies.

Among the adsorbed proteins on anti-proliferative microparticles, only a few proteins, such as collagen III, galectin, and desmoglein 4, are associated with wound healing. Although collagen is a significant structural protein, its overexpression may lead to fibrous and scar tissue formation. As wound healing progresses from the inflammatory phase to the proliferation and remodelling phases, the amount of collagen III at the site of injury decreases while collagen I increases. Their ratio determines the final fibril size and geometry of the healed wound.[72] Therefore, any mechanism disturbing the collagen I/collagen III ratio might lead to impaired wound healing. Besides, galectin, which is implicated in hypertrophic scar formation by causing hyperproliferation of fibroblasts and over-secretion of collagen, was adsorbed on anti-proliferative microparticles.[73] Desmoglein 4 on the other hand coordinates the proliferation and differentiation of hair follicle keratinocytes and its deficiency stimulates an immune-mediated skin condition.[74,75] Whilst this report focuses on protein adsorption to the surface of biomaterials, it is important to highlight that bio-active peptides have also been shown to play an important role in the bio-interface for wound healing, which can be used as biotherapeutics.[76–78]

While it is challenging to determine the particular effects of individual proteins, it is clear that surface chemistry determines the adsorbed protein type. These uniquely adsorbed proteins can alter the cell–biomaterial interactions, leading to enhanced fibroblast activity and better wound healing.

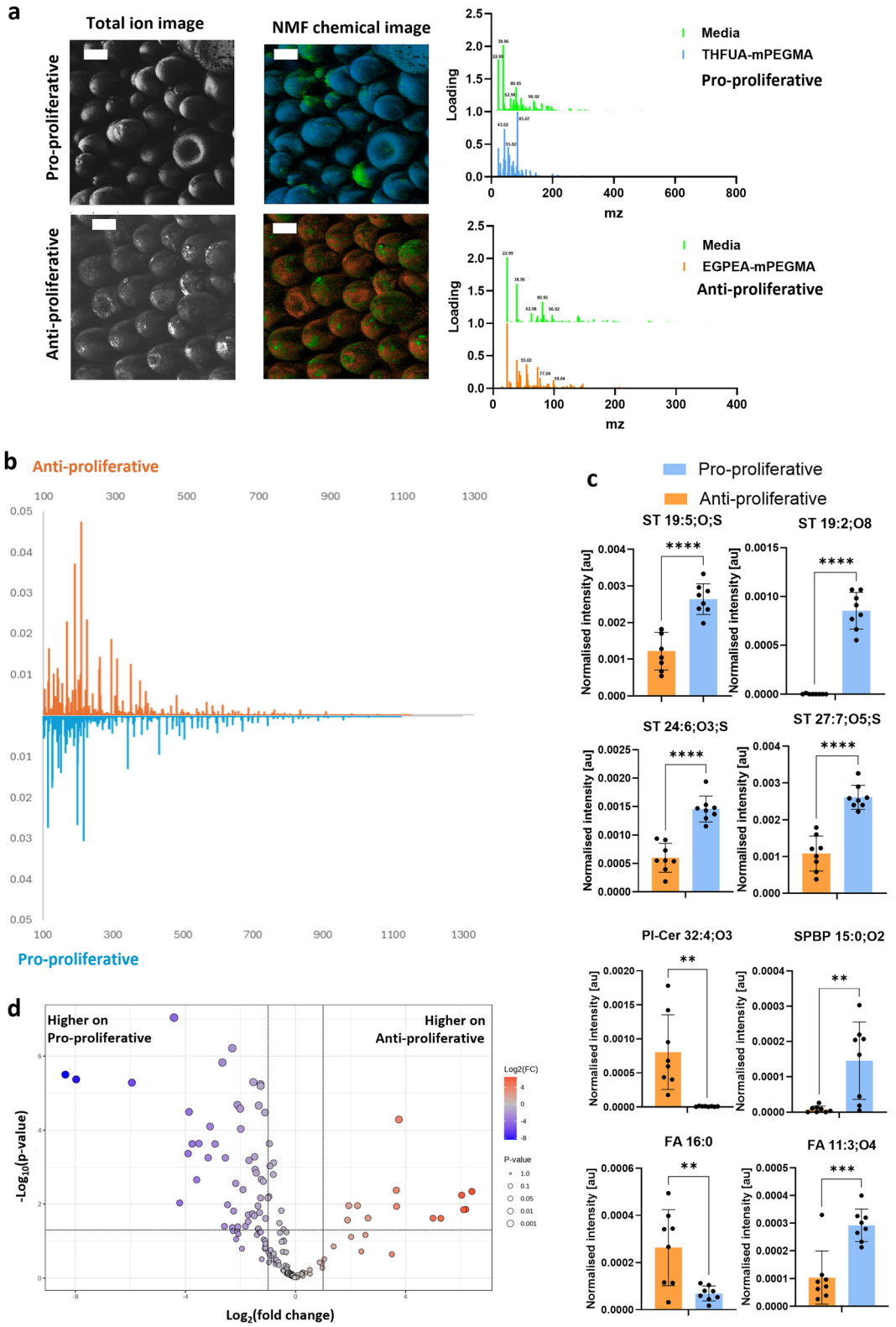

Fig. 6 Lipid deposition on microparticles. (a) NMF loadings showing the separation of ToF-SIMS data into two distinct components: media and polymer after 300 iterations. Scale bar: 20 μm. (b) Orbi-SIMS spectra of lipids in positive polarity mode adsorbed on anti-proliferative (EGPEA-*co*-mPEGMA$_{300}$, top, orange) and pro-proliferative microparticles (THFuA-*co*-mPEGMA$_{300}$, bottom, blue) identified using MFP. (c) Normalized intensity to total ion count of the top 8 most abundant lipids significantly adsorbed on anti-proliferative and pro-proliferative microparticles. Data are presented as mean ± SD (n = 8). **p < 0.01, ***p < 0.001, ****p < 0.0001. (d) Volcano plot of lipid species identified on anti-proliferative and pro-proliferative microparticles by Orbi-SIMS analysis in both positive and negative polarity modes. Each point represents one lipid. Data are presented as the mean of n = 8.

2.4. Identification of lipid deposition/retention on cell-instructive microparticles

To gain insight into the preferential lipid deposition/retention on these materials to complement the proteomic data, microparticles were incubated overnight in the same type of cell culture medium that was used for the proteomics study (without cells). This medium was supplemented with 10% FBS, comprises 0.19 mM fatty acids, 0.04 mM polyunsaturated fatty acids, and 0.09 mM cholesterol.[79] Following washing in PBS and ultrapure water, the microparticles were dried under argon flow and ToF-SIMS images were acquired. The multivariate analytical approach of NMF (non-negative matrix factorization) was used to identify two major phases in the images, namely the polymer and the medium components.

The components of the medium adsorbed and retained on microparticles are shown in green in Fig. 6a, whereas the polymer chemistries have been colored as orange (EGPEA-*co*-mPEGMA$_{300}$) and blue (THFuA-*co*-mPEGMA$_{300}$). It can be seen from Fig. 6a that there is a heterogeneous deposition of medium components on the surface of microparticles. For molecular assignment of individual components, Orbi-SIMS was used since it has superior mass resolving power for the detection of biomolecules compared to ToF-SIMS.[14] Orbi-SIMS analysis, using the molecular formula prediction (MFP) analysis protocol,[80] is used to focus on the lipid component of the spectra. The structures of lipids that displayed significant differential adsorption on the biomaterials are displayed within the Orbi-SIMS spectra (Fig. 6b). Their signals are relatively low in intensity compared to the surrounding polymer peaks, but they are statistically significant ($p < 0.0001$).

The detected lipid species were categorized into fatty acids (FA), glycerolipids (GL), glycerophospholipids (GP), sphingolipids (SP), and sterols (ST). Fig. S9 (SI) presents a heat map illustrating color-scaled intensities of lipid groups detected on anti-proliferative and pro-proliferative microparticles. The volcano plot shown in Fig. 6d illustrates differential deposition of lipids on anti- and pro-proliferative microparticles. The ion intensities of detected lipids on each microparticle were analyzed comparatively and the eight most abundant lipids, which exhibit significantly different adsorption behavior on anti- and pro-proliferative microparticles, are shown in Fig. 6c. The ion intensity of sterols on microparticles, particularly the pro-proliferative ones, was relatively high compared to that on the anti-proliferative materials. Sterols play an important role in biological processes such as inflammation and healing. For example, cholesterol regulates inflammation and maintains the skin barrier.[12] Liu *et al.* reported that β-sitosterol treatment facilitates wound healing in diabetic rats by promoting collagen synthesis, angiogenesis, and M2 macrophage proliferation.[81]

The lipid species SPBP 15 : 0;O2 (sphingoid base phosphate), from the sphingolipid (SP) family, was detected on the surface of pro-proliferative microparticles at a significantly higher intensity compared to that on anti-proliferative microparticles. Sphingolipids have been reported to play a cardinal role in the regulation of wound healing and fibrosis in various organs, including the skin, eye, and lungs, *via* influencing fibroblast migration, differentiation, and TGF-β signaling.[82] Aoki *et al.* recently demonstrated that the topical treatment of sphingosine-1-phosphate (S1P) enhanced wound healing in S1P-deficient mice by promoting the recruitment of immune cells and angiogenesis.[83] It was observed that the anti- and pro-proliferative microparticles exhibit varying lipid deposition profiles, resulting in a distinct characteristic at the bio-interface. The functions of abundantly adsorbed sterols and sphingolipids on pro-proliferative microparticles, in tandem with the adsorbed protein species, may play a pivotal role in wound healing. This would align with the intended use of pro-proliferative microparticles.

3. Conclusions

This study investigated the interaction between cell-instructive microparticles and skin fibroblasts *in vitro* for wound healing. Microparticles with a biodegradable P$_{DL}$LA core and fibroblast-instructive surface chemistries were fabricated (ø = 20–30 μm) with a uniform surface chemistry, which adhered to the surface for a minimum of 21 days, and were characterized using ToF-SIMS. It was shown that fibroblasts established cellular connections between the microparticles that facilitated cell elongation and proliferation *in vitro*, and perhaps assisted in the healing process *in vivo*. *In vitro* wound healing was accelerated on treatment with pro-proliferative microparticles that promote cell proliferation. Cell motility, bridge formation and tumbling behaviors were observed and postulated to be at least partly responsible. Proteins that are uniquely adsorbed onto pro- or anti-inflammatory surfaces were identified, providing insights into the potential processes by which these materials speed up wound healing. Annexin, olfactomedin 4, and vimentin were adsorbed through surface chemistries that promote cell proliferation. Lipid depositions on microparticles were also investigated, and sterol species were found to have significantly higher adsorption on pro-proliferative microparticles compared to that on anti-proliferative microparticles. This is the first step in further understanding the bio-interface of these new bio-instructive polymers to elucidate the relationship between polymer structure and biological performance. The literature on these bio interfacial molecular observations supports the notion of accelerated healing.

4. Experimental section

4.1. Materials

1,6-Hexanediol diacrylate (HMDA, 80%) fibroblast-instructive monomers previously identified *via* a HT technique, ethylene glycol phenyl ether acrylate (EGPEA), tetrahydrofurfuryl acrylate (THFuA)[84] and ethylene glycol methyl ether methacrylate (mPEGMA) (M_n = 300 g mol^{-1}) monomers were supplied by Sigma-Aldrich. The initiator of CCTR, 2,2-azobis(2-methyl-

propionitrile) (AIBN, 98%) was also provided by Sigma-Aldrich, while the catalytic chain transfer agent bis[(difluoroboryl) diphenylglyoximato] cobalt(II) (PhCoBF) was purchased from DuPont. The solvents, cyclohexanone (Scientific Laboratory Supplies) and hexane (VWR Chemicals), were used, as received, in synthesis and precipitation, respectively. Unless noted otherwise, all supplies were used exactly as delivered.

4.2. Surfactant synthesis

The polymer surfactants used in this study were synthesized using catalytic chain transfer polymerization as described in a previously developed protocol.[36] The monomers were added in the required quantities to achieve the desired molar ratios (ThFuA/EGPEA : $mPEGMA_{300}$, 90 : 10%, mol : mol) into a reaction vial containing cyclohexanone with a 1 : 3 (v/v) monomer : solvent ratio. A requisite volume of PhCoBF stock solution in cyclohexanone (2 mg mL^{-1}) was added to the reaction vial to achieve a final concentration of 700 ppm. Finally, AIBN (0.5% w/w of the total monomer) initiator was added, and the vial was sealed. The reaction vial was immersed in an ice bath to prevent initiating the reaction and was degassed under argon flow for at least 1 hour using a Schlenk line. The reaction was started by placing the reaction vessel in an oil bath at 85 °C for 18 hours and agitating the reaction mixture during this time. Purification was done by precipitating the reaction product in an excess amount of hexane (nonsolvent : reaction, 5 : 1 v/v). Then, the precipitated products were collected in a vial and kept in a vacuum oven for 1 week to remove any remaining solvent. The reaction conversion was identified by analyzing the crude product using NMR spectroscopy, while the actual monomer ratio of the final copolymer composition was determined *via* the purified product. The molecular weights of products were evaluated *via* GPC analysis of the purified samples dissolved in HPLC grade THF.

^1H nuclear magnetic resonance analysis: ^1H NMR spectra were collected using a Bruker DPX-300 spectrometer (400 MHz) at 25 °C. Samples were prepared by dissolving in deuterated chloroform ($CDCl_3$) and chemical shifts are referenced to residual $CDCl_3$ at 7.26 ppm.

Gel permeation chromatography analysis: Agilent 1260 Infinity equipment was used to conduct GPC analysis. The equipment contained a dual detector and a light-scattering setup. Tetrahydrofuran (THF) was used as the mobile phase at a flow rate of 1 mL min^{-1} in two mixed columns at 25 °C. GPC samples were prepared by dissolving in HPLC-grade THF and filtered prior to injection into the column. The analysis was done *via* Astra software. The polydispersity ($Đ$) and number average molecular weight (M_n) were determined using PMMA for the calibration curve.

THFuA-*co*-$mPEGMA_{300}$: M_n (GPC): 14 900 $gmol^{-1}$, $Đ$: 2.22, actual monomer ratio was 91 : 9 mol : mol THFuA : $mPEGMA_{300}$.

EGPEA-*co*-$mPEGMA_{300}$: M_n (GPC): 19 700 $gmol^{-1}$, $Đ$: 2.56, actual molar ratio was 87 : 13 mol : mol EGPEA : $mPEGMA_{300}$.

4.3. Low MW $P_{DL}LA$ synthesis

Low molecular weight lactic acid was synthesised by following a previously published work.[37] Lactic acid and initiator (Geraniol) were dissolved in a pre-dried vial containing dry dichloromethane at a 10 : 1 monomer : initiator ratio. The catalyst, 1,8-diazabicyclo[5.4.0]undec-7-ene (DBU), was added with a 1.5% (mol : mol) catalyst : monomer ratio. The reaction was performed at room temperature for 30 minutes. Then the reaction product was precipitated in cold 1 : 1 diethyl ether:40–60 °C petroleum ether mixture in an ice bath. The organic solvent was removed by centrifuging at 4000 rpm for 10 minutes, and the reaction product was placed in a vacuum oven to acquire the final oligomer as a white solid. M_n (GPC) 2209 Da, DP = 13 and $Đ$ 1.2.

4.4. Microparticle production

Microparticles were fabricated using a 2-reagent hydrophilic multichannel microfluidic chip and a Telos® high-throughput system produced by Dolomite Microfluidics (Cambridge, UK). Pumps pressuring the fluids and the outlet of the collection vessel were connected to the system *via* polytetrafluoroethylene tubing with inner diameter 250 μm and outer diameter 1.6 mm. The dispersed phase was prepared by dissolving 5% (w/v) biodegradable polymer and 0.1% (w/w) polymer surfactant in ethyl acetate (Merck). The biodegradable polymer contained 75% (w/w) poly(D,L-lactic acid) ($P_{DL}LA$, M_n 47 000 g mol^{-1}), supplied by Evonik Rohm GmbH (Darmstadt, Germany), and 25% (w/w) low molecular weight PDLLA synthesized as described in a previous study.[37] The dispersed phase solution was degassed in an ultrasonic bath and introduced to a microfluidic chip at a target flow rate of 10–15 mL min^{-1}. The continuous phase contained 0.1% polyvinyl alcohol (PVA, 88% hydrolyzed) (Fisher Chemicals) for experiments producing particles with EGPEA-*co*-$mPEGMA_{300}$ and THFuA-*co*-$mPEGMA_{300}$ polymer surfactants while the continuous phase was 2% PVA for experiments not using polymer surfactants in the dispersed phase. The continuous phase flow rate was 400–450 mL min^{-1}. Emulsion droplets were collected in a cylindrical vessel containing excess distilled water to provide sufficient time for the diffusion of ethyl acetate and the formation of solid microparticles with a $P_{DL}LA$ core. Microparticles were centrifuged for full removal of water before SEM and ToF-SIMS analysis.

4.5. Characterization

SEM imaging was performed using a Hitachi TM3030 table-top SEM. Dried particles were scattered onto double-sided adhesive carbon tape on a sample holder, followed by 90-second, 25 mA gold coating in an argon environment to enhance electron conductivity. ImageJ software was utilized for size measurements by analyzing the diameters of at least hundreds of samples captured at ×150 magnification in three regions of interest.

The surface chemistry of microparticles was evaluated using a ToF-SIMS IV instrument (IONTOF GmbH, Münster, Germany). Microparticles were sprinkled on a poly(hydroxyethyl) methacrylate substrate and mass spectrometry analysis was performed by conducting 500 μm × 500 μm scans with a

Bi_3^+ primary ion source. Ion-ToF software was used to calibrate and analyze the spectra.[85]

4.6. Cell culture

Human skin fibroblasts (CRL-2522, ATCC) were grown in minimum essential medium (MEM, Eagle), which included foetal bovine serum (10%), L-glutamine (1%), non-essential amino acids (1%), penicillin/streptomycin (1%), and sodium pyruvate (1%). All components of the medium were purchased from Sigma. Before passaging or seeding, the fibroblasts were cultured in T75 flasks at 37 °C under 5% CO_2 until reaching 90% confluency.

4.7. Fibroblast attachment and proliferation on microparticles

The number of attached cells on the microparticles at 24 h and 96 h of culture was determined using the CyQuant NF assay (Thermo Fisher). This assay approach involved measuring the fluorescence intensity of DNA dye binding, which is proportional to cellular DNA content, to determine the cell number. The cell number of the sample was calculated by comparing the fluorescence intensity of the sample against the fluorescence intensity of the known cell number. Fibroblast proliferation was studied *via* the cell proliferation ELISA (colorimetric, Roche). This assay measured 5-bromo-2′-deoxyuridine (BrdU) dye incorporation during DNA synthesis to quantify cell proliferation. The assay was performed according to the manufacturer's instructions. Results were represented as stimulation index (SI), calculated by dividing the optical density of stimulated cells (treated with particles) by the optical density of unstimulated cells (non-treated with particles).

4.8. Wound healing assay

IBIDI 4-compartment silicone inserts were used to perform an *in vitro* wound healing assay on a tissue culture plate (TCP) by creating a wound gap. Briefly, cells were seeded in the insert compartments, and after the cells had reached confluence, the insert was carefully removed. The cell layer was washed twice with fresh medium to remove any remaining cell debris and cultured in fresh medium for up to 96 hours with and without microparticles. At certain time points (12, 24, 48, 72 and 96 hours), microparticles were removed and cells were fixed and stained with HCS CellMask Green (ThermoFisher Scientific). The imaging was performed using an Etaluma LS720 microscope (Carlsbad, CA, USA). The wound closure percentage was determined by quantifying the area covered by fibroblasts within the initial wound gap area using Fiji ImageJ software. Cell proliferation was assessed by calculating the percentage of Ki67 (Abcam, ab16667) antibody-positive cells at 48, 72 and 96 hours of wound healing. Ki-67 is detected in the cell cycle phases including cell growth and DNA synthesis. The cells were washed twice with phosphate-buffered saline (PBS) solution and fixed with 4% paraformaldehyde for 15 minutes. After permeabilizing with 0.1% Triton X-100 for 15 minutes, the cells were blocked with a solution containing (1%) BSA, (10%) normal goat serum, (0.3M) glycine, (0.1%) Tween in PBS for 1 hour. Then antibody staining was completed by incubating cells in Ki67 antibody (Abcam) at 1/250 dilution in PBS overnight at 4 °C. After washing the samples twice with (0.2%) Tween-PBS solution, secondary antibody staining was done by incubating with goat anti-rabbit IgG H&L (Alexa Fluor® 488) at room temperature for 1 hour. Cell nuclei were stained with DAPI.

4.9. Cytokine quantification assay

After culturing fibroblasts on microparticles for 96 hours, the concentrations of growth factors (bFGF, HGF) and cytokines (IL-6, MCP-1) secreted into the culture medium were measured using Duoset ELISA kits (R&D Systems) as specified in the manufacturer's instructions.

4.10. Protein identification

The identification of adsorbed proteins on microparticle surfaces was carried out by following the method in previously published works.[23,59] Briefly, microparticle samples were incubated in 4-well TCP in (4 mL) complete medium (10% FBS, 1% penicillin/streptomycin, L-glutamine, MEM non-essential amino acid solution, and sodium pyruvate solution) overnight at 37 °C. After removing the medium, samples were gently rinsed with PBS and then with ultrapure water. Then samples were incubated in extraction solution (200 mL) containing sodium chloride (1 M), urea (6 M), Triton X-100 (1%), and isopropyl alcohol (50%) for 1 hour at room temperature on a platform shaker (10 rpm). Then, the extraction solution was transferred into an Eppendorf tube and 800 mL of cold acetone was added. After incubating at −20 °C for 1 hour, the acetone was removed by centrifuging at 4 °C for 10 minutes (13 000*g*). Protein pellets were dissolved in 10 mL of ultrapure water and combined for each sample. Pierce BCA Protein Assay (Thermo Scientific, USA) was utilized to evaluate concentrations of adsorbed proteins using BSA as the protein standard. Then the extracted proteins were separated according to molecular weights *via* SDS-PAGE analysis on 4-polyacrylamide gels (15%) for 1 hour at 120 V. After staining the obtained gel with the Pierce Silver Stain kit (Thermo Scientific) by following the manufacturer's instructions, protein bands were cut with the help of a scalpel. The protein bands were stored at −20 °C.

4.11. Liquid chromatography-tandem mass spectrometry analysis

Proteins in gel bands were further investigated by liquid chromatography-tandem mass spectrometry (LC-MS/MS). Following reduction, alkylation and digestion of the protein samples with trypsin, a Dionex Ultimate 3000 RSLC nanoUPLC system (Thermo Fisher Scientific Inc., Waltham, MA, USA) and an Orbitrap Fusion Lumos mass spectrometer (Thermo Fisher Scientific Inc., Waltham, MA, USA) were utilised to perform all LC-MS/MS experiments.

The peptides were introduced onto a pre-column (Thermo Scientific PepMap 100 C18, 5 μm particle size, 100 Å pore size, 300 μm i.d. × 5 mm length) using the Ultimate 3000 auto-

sampler. The introduction process involved the use of 0.1% formic acid for a duration of 3 minutes, with a flow rate of 15 μL min^{-1}. Then, the column valve was adjusted to enable the elution of peptides from the pre-column into the analytical column. The peptides were separated using C18 reverse-phase chromatography and a Thermo Scientific reverse-phase nano Easy-spray column (Thermo Scientific PepMap C18, 2 μm particle size, 100 Å pore size, 75 μm i.d. × 50 cm length). The flow rates of both columns were 300 nL min^{-1}. Solvent A consisted of a mixture of water and 0.1% formic acid, while solvent B was composed of 80% acetonitrile, 20% water, and 0.1% formic acid. The utilized linear gradient ranged from 2% to 40% B during a period of 30 minutes. The total duration of the LC run was 60 minutes, which included the high organic washing step and column re-equilibration.

The peptides that were separated from the C18 column LC eluent were introduced into the mass spectrometer using an Easy-Spray source manufactured by Thermo Fisher Scientific Inc. The *m*/*z* values of eluting peptide ions were determined using an Orbitrap mass analyzer, which was set to a resolution of 120 000. The scan range for the measurements was between *m*/*z* 380 and 1500 Da. The experiment utilized data-dependent MS/MS scans with a cycle time of 3 seconds to autonomously isolate and fragment precursor ions, generating fragment ions through higher energy collisional-induced dissociation (HCD) with a normalized collision energy (NCE) of 32% in the ion routing multipole. The Orbitrap's resolution was configured to 15 000 for the measurement of fragment ions. Ions with a single charge, ions with more than seven charges and ions with unknown charge states were excluded. Additionally, a dynamic exclusion window of 70 seconds was used.

The data obtained from MS/MS were converted to .mgf file format and submitted to the Mascot search algorithm (Matrix Science, London UK, version 2.6.0). A database search was carried out against the UniProt bovine database (Bos_taurus_20200106, 37 880 entries) and common contaminant sequences (126 sequences; 41 577 residues). The mass tolerances for peptide and fragment were established at 20 ppm and 0.1 Da, respectively. The peptide cutoff score was set to 20 and the significance threshold value was $p < 0.5$. The lists of proteins for each band pair representing the same molecular weights were compared manually. Then the unique proteins of each sample in band pairs were identified and combined to obtain uniquely adsorbed protein lists for each surface chemistry. The protein abundance was determined by its exponentially modified protein abundance index (emPAI) obtained from the Mascot algorithm search.

4.12. Lipid identification

Microparticles were placed into vials and subjected to UV sterilization for 20 minutes. Following a brief rinse with distilled water and PBS, microparticles were incubated in complete MEM at 37 °C for 24 hours. The medium was removed, and the microparticles were quickly washed with PBS and ultrapure water. Microparticles were desiccated under argon flow for one hour to avert oxygen exposure and stored at −17 °C until analysis. This process was implemented to reduce the likelihood of lipid peroxidation on the surface of the microparticles. Prior to the Orbi-SIMS analysis, microparticles were secured to the back-mount holders with copper tape. The samples were exposed to a continuous flow of inert nitrogen gas to eliminate any loose microparticles before being introduced into the instrument.

4.13. 3D Orbi-SIMS analysis

The HybridSIMS instrument (IONTOF, GmbH) set to Mode 4 (single beam 20 keV Ar_{3000}^+, OrbitrapTM analyzer) was used to perform the analysis. The instrument used an Ar_{3000}^+ primary ion beam of energy 20 keV for a duty cycle of 4.4% and a continuous GCIB current of 230 pA, over an area of 300 × 300 μm^2 with a crater size of 381.8 × 381.8 μm^2. Mass spectra information was collected over the range of 75–1125 *m*/*z*. The electron flood gun was operated with 21 eV energy and 20 V extraction bias for charge compensation. The injection time was maintained at 500 ms. The total ion dose per measurement was set as 3.95×10^{11} ions per cm^2. The pressure in the chamber was set to 1.6×10^{-6} mbar. The analysis was performed in both negative and positive polarities using the Q Exactive HF operating at a mass resolution setting of 240 000 (at *m*/*z* 200), to collect secondary ions. Data were analyzed and exported using the SurfaceLab software version 7.1 (ION-TOF, Germany). Molecular formula prediction (MFP) and chemical filtering were conducted using SIMS-MFP software, which was created in MATLAB.[80] Then, negative matrix factorization (NMF) was applied using the SIMS-MFP software.

4.14. ToF-SIMS analysis

ToF-SIMS analysis was also performed on the samples using a ToF-SIMS IV instrument (IONToF, GmbH, Munster, Germany) with a bismuth cluster primary ion source (30 keV Bi_3^+) with both negative and positive polarities. The cycle time was 150 μs. The analysis area was set as 150 μm × 150 μm.

4.15. Statistical analysis

All data were presented as mean ± standard deviation. Biological and technical replicates were indicated as *N* and *n*. The statistical significance of normalized intensity to total ion count of the top 8 most abundant lipids was calculated by the unpaired two-tailed *t*-test. The rest of the statistical significances were determined using a one-way analysis of variance (ANOVA) and Tukey's *post hoc* analysis using GraphPad Prism 10.2.3. A *p*-value of ≤0.1 was regarded as statistically significant.

Conflicts of interest

The authors declare no conflict of interest.

Data availability

The data supporting the findings of this study are available in the University of Nottingham data repository at **https://doi.org/10.17639/nott.7504**.

Supplementary information is available. SI for this study, including surfactant characterization, cell viability, attachment, degradation data, and protein and lipid lists, is available from DOI: **https://doi.org/10.1039/d5bm00896d**.

Acknowledgements

This work was funded by the Engineering and Physical Sciences Research Council (grant reference EP/X001156/1). Zeynep Imir Tekneci acknowledges the Republic of Türkiye Ministry of National Education for the funding of her PhD studentship at the University of Nottingham. The authors acknowledge The Cambridge Center for Proteomics for the LC-MS/MS service analysis of surface-extracted proteins. Anna M. Kotowska is acknowledged for her help with Orbi-SIMS analysis.

References

1 P. Kolimi, S. Narala, D. Nyavanandi, A. A. A. Youssef and N. Dudhipala, *Cells*, 2022, **11**, 2439.
2 M. Rodrigues, N. Kosaric, C. A. Bonham and G. C. Gurtner, *Physiol. Rev.*, 2019, **99**, 665.
3 H. E. Talbott, S. Mascharak, M. Griffin, D. C. Wan and M. T. Longaker, *Cell Stem Cell*, 2022, **29**, 1161.
4 G. C. Gurtner, S. Werner, Y. Barrandon and M. T. Longaker, *Nature*, 2008, **453**, 314.
5 S. Patel, S. Srivastava, M. R. Singh and D. Singh, *Biomed. Pharmacother.*, 2019, **112**, 108615.
6 N. X. Landén, D. Li and M. Ståhle, *Cell. Mol. Life Sci.*, 2016, **73**, 3861–3885.
7 E. Santos-Vizcaino, A. Salvador, C. Vairo, M. Igartua, R. M. Hernandez, L. Correa, S. Villullas and G. Gainza, *Nanomaterials*, 2020, **10**, 1.
8 S. Beyaz, Ü. Ö. Güler and G. Ş. Bağır, *Acta Orthop. Traumatol. Turc.*, 2017, **51**, 393.
9 R. Maheswaran, T. Tong, J. Michaels, P. Brindley, S. Walters and S. Nawaz, *BJS Open*, 2024, **8**(1), DOI: **10.1093/BJSOPEN/ZRAD140**.
10 E. N. Mpoyi, M. Cantini, P. M. Reynolds, N. Gadegaard, M. J. Dalby and M. Salmerón-Sánchez, *ACS Nano*, 2016, **10**, 6638.
11 M. D. Swartzlander, C. A. Barnes, A. K. Blakney, J. L. Kaar, T. R. Kyriakides and S. J. Bryant, *Biomaterials*, 2015, **41**, 26.
12 V. Choudhary, M. Choudhary and W. B. Bollag, *Int. J. Mol. Sci.*, 2024, **25**(7), 3790.
13 C. C. Schreib, M. I. Jarvis, T. Terlier, J. Goell, S. Mukherjee, M. D. Doerfert, T. A. Wilson, M. Beauregard, K. N. Martins, J. Lee, L. D. Sanchez Solis, E. Vazquez, M. A. Oberli, B. W. Hanak, M. Diehl, I. Hilton and O. Veiseh, *Adv. Mater.*, 2023, **35**(21), DOI: **10.1002/ADMA.202205709**.
14 M. K. Passarelli, A. Pirkl, R. Moellers, D. Grinfeld, F. Kollmer, R. Havelund, C. F. Newman, P. S. Marshall, H. Arlinghaus, M. R. Alexander, A. West, S. Horning, E. Niehuis, A. Makarov, C. T. Dollery and I. S. Gilmore, *Nat. Methods*, 2017, **14**(12), 1175.
15 W. Suvannapruk, L. E. Fisher, J. C. Luckett, M. K. Edney, A. M. Kotowska, D. H. Kim, D. J. Scurr, A. M. Ghaemmaghami and M. R. Alexander, *Adv. Sci.*, 2024, **11**, 1.
16 R. M. Visalakshan, M. N. Macgregor, S. Sasidharan, A. Ghazaryan, A. M. Mierczynska-Vasilev, S. Morsbach, K. Landfester, J. D. Hayball and K. Vasilev, *ACS Appl. Mater. Interfaces*, 2019, **11**(31), 27615–27623.
17 O. Veiseh, J. C. Doloff, M. Ma, A. J. Vegas, H. H. Tam, A. R. Bader, J. Li, E. Langan, J. Wyckoff, W. S. Loo, S. Jhunjhunwala, A. Chiu, S. Siebert, K. Tang, J. Hollister-Lock, S. Aresta-Dasilva, M. Bochenek, J. Mendoza-Elias, Y. Wang, M. Qi, D. M. Lavin, M. Chen, N. Dholakia, R. Thakrar, I. Lacík, G. C. Weir, J. Oberholzer, D. L. Greiner, R. Langer and D. G. Anderson, *Nat. Mater.*, 2015, **14**, 643.
18 A. J. Vegas, O. Veiseh, J. C. Doloff, M. Ma, H. H. Tam, K. Bratlie, J. Li, A. R. Bader, E. Langan, K. Olejnik, P. Fenton, J. W. Kang, J. Hollister-Locke, M. A. Bochenek, A. Chiu, S. Siebert, K. Tang, S. Jhunjhunwala, S. Aresta-Dasilva, N. Dholakia, R. Thakrar, T. Vietti, M. Chen, J. Cohen, K. Siniakowicz, M. Qi, J. McGarrigle, S. Lyle, D. M. Harlan, D. L. Greiner, J. Oberholzer, G. C. Weir, R. Langer and D. G. Anderson, *Nat. Biotechnol.*, 2016, **34**(3), 345.
19 A. Vishwakarma, N. S. Bhise, M. B. Evangelista, J. Rouwkema, M. R. Dokmeci, A. M. Ghaemmaghami, N. E. Vrana and A. Khademhosseini, *Trends Biotechnol.*, 2016, **34**(6), 470–482.
20 Y. Wang, X. Zhang, D. Xie, C. Chen, Z. Huang and Z. A. Li, *Adv. Funct. Mater.*, 2025, **35**, 2419610.
21 J. Hu, Y. Li, Z. Cai, H. Wang, J. Li, S. Wang, X. Liu, S. Pang, P. Zhang, T. Lou, C. Zhou, S. Liu and C. Fan, *Int. J. Biol. Macromol.*, 2025, **319**, 145631.
22 A. L. Hook, D. G. Anderson, R. Langer, P. Williams, M. C. Davies and M. R. Alexander, *Biomaterials*, 2010, **31**, 187.
23 H. M. Rostam, L. E. Fisher, A. L. Hook, L. Burroughs, J. C. Luckett, G. P. Figueredo, C. Mbadugha, A. C. K. Teo, A. Latif, L. Kämmerling, M. Day, K. Lawler, D. Barrett, S. Elsheikh, M. Ilyas, D. A. Winkler, M. R. Alexander and A. M. Ghaemmaghami, *Matter*, 2020, **2**, 1564.
24 A. A. Dundas, O. Sanni, J. F. Dubern, G. Dimitrakis, A. L. Hook, D. J. Irvine, P. Williams and M. R. Alexander, *Adv. Mater.*, 2019, **31**(49), DOI: **10.1002/ADMA.201903513**.
25 A. Latif, L. E. Fisher, A. A. Dundas, V. Cuzzucoli Crucitti, Z. Imir, K. Lawler, F. Pappalardo, B. W. Muir, R. Wildman, D. J. Irvine, M. R. Alexander and A. M. Ghaemmaghami, *Adv. Mater.*, 2022, **36**(43), 2208364, DOI: **10.1002/adma.202208364**.
26 J. Yang, F. R. A. J. Rose, N. Gadegaard and M. R. Alexander, *Adv. Mater.*, 2009, **21**, 300.

27 E. Capuana, F. Lopresti, M. Ceraulo and V. La Carrubba, *Polymers*, 2022, **14**, 1.
28 D. Da Silva, M. Kaduri, M. Poley, O. Adir, N. Krinsky, J. Shainsky-Roitman and A. Schroeder, *Chem. Eng. J.*, 2018, **340**, 9–14.
29 C. Zhu, H. Yang, L. Shen, Z. Zheng, S. Zhao, Q. Li, F. Yu and L. Cen, *J. Biomater. Sci., Polym. Ed.*, 2019, **30**, 737.
30 P. Blasi, *J. Pharm. Invest.*, 2019, **49**, 337.
31 K. Keohane, D. Brennan, P. Galvin and B. T. Griffin, *Int. J. Pharm.*, 2014, **467**(1–2), 60–69.
32 J. M. Anderson and M. S. Shive, *Adv. Drug Delivery Rev.*, 2012, **64**, 72–82.
33 C. A. Henshaw, A. A. Dundas, V. Cuzzucoli Crucitti, M. R. Alexander, R. Wildman, F. R. A. J. Rose, D. J. Irvine and P. M. Williams, *Molecules*, 2021, **26**, 3302.
34 V. Cuzzucoli Crucitti, L. Contreas, V. Taresco, S. C. Howard, A. A. Dundas, M. J. Limo, T. Nisisako, P. M. Williams, P. Williams, M. R. Alexander, R. D. Wildman, B. W. Muir and D. J. Irvine, *ACS Appl. Mater. Interfaces*, 2021, **13**, 43300.
35 K. W. A. Lee, L. K. W. Chan, A. W. K. Lee, C. H. Lee, S. T. H. Wong and K.-H. Yi, *Polymers*, 2024, **16**, 2583.
36 A. A. Dundas, V. Cuzzucoli Crucitti, S. Haas, J. F. Dubern, A. Latif, M. Romero, O. Sanni, A. M. Ghaemmaghami, P. Williams, M. R. Alexander, R. Wildman and D. J. Irvine, *Adv. Funct. Mater.*, 2020, **30**, 2001821.
37 D. M. O'Brien, R. L. Atkinson, R. Cavanagh, A. A. C. Pacheco, R. Larder, K. Kortsen, E. Krumins, A. J. Haddleton, C. Alexander, R. A. Stockman, S. M. Howdle and V. Taresco, *Eur. Polym. J.*, 2020, **125**, 109516.
38 T. Velnar, T. Bailey and V. Smrkolj, *J. Int. Med. Res.*, 2009, **37**, 1528.
39 *Advanced Wound Repair Therapies*, ed. D. Farrar, In Woodhead Publishing Series in Biomaterials, 2011.
40 R. F. Pirlar, M. Emaneini, R. Beigverdi, M. Banar, W. B. van Leeuwen and F. Jabalameli, *PLoS One*, 2020, **15**, e0235093.
41 C. Pouget, C. Dunyach-Remy, T. Bernardi, C. Provot, J. Tasse, A. Sotto and J. P. Lavigne, *Front. Microbiol.*, 2022, **13**, 1.
42 A. Latif, L. E. Fisher, A. A. Dundas, V. Cuzzucoli Crucitti, Z. Imir, K. Lawler, F. Pappalardo, B. W. Muir, R. Wildman, D. J. Irvine, M. R. Alexander and A. M. Ghaemmaghami, *Adv. Mater.*, 2022, 2208364.
43 G. E. Visscher, R. L. Robison, H. V. Maulding, J. W. Fong, J. E. Pearson and G. J. Argentieri, *J. Biomed. Mater. Res.*, 1986, **20**(5), 667–676.
44 M. Ayushman, G. Mikos, X. Tong, S. Sinha, E. Lopez-Fuentes, S. Jones, P. C. Cai, H.-P. Lee, A. J. Morrison, A. Spakowitz, S. C. Heilshorn, A. Sweet-Cordero and F. Yang, *Nat. Mater.*, 2024, **2024**, 1.
45 B. G. Zani and E. R. Edelman, *Commun. Integr. Biol.*, 2010, **3**, 215.
46 I. Benjumeda Wijnhoven, R. Vallejos, J. F. Santibanez, C. Millán and J. F. Vivanco, *Sci. Rep.*, 2020, **10**, 1.
47 H. Eagle and E. M. Levine, *Nature*, 1967, **213**, 1102, 5081.
48 X. Sun and P. D. Kaufman, *Chromosoma*, 2018, **127**, 175–186.
49 S. L. Deshmane, S. Kremlev, S. Amini and B. E. Sawaya, *J. Interferon Cytokine Res.*, 2009, **29**, 313.
50 H. Eagle and E. M. Levine, *Nature*, 1967, **213**, 1102, 5081.
51 X. Sun and P. D. Kaufman, *Chromosoma*, 2018, **127**, 175–186.
52 S. L. Deshmane, S. Kremlev, S. Amini and B. E. Sawaya, *J. Interferon Cytokine Res.*, 2009, **29**, 313.
53 P. Chomarat, J. Banchereau, J. Davoust and A. K. Palucka, *Nat. Immunol.*, 2000, **1**(6), 510.
54 M. Farooq, A. W. Khan, M. S. Kim and S. Choi, *Cells*, 2021, **10**(11), 3242.
55 K. Conway, P. Price, K. G. Harding and W. G. Jiang, *Wound Repair Regener.*, 2008, **14**(1), 2–10.
56 D. Bevan, E. Gherardi, T.-P. Fan, D. Edwards and R. Warn, *J. Pathol.*, 2004, **203**, 831.
57 X. Yi, X. Li, Y. Zhou, S. Ren, W. Wan, G. Feng and X. Jiang, *Int. J. Mol. Med.*, 2014, **34**, 381.
58 D. P. Myatt, *Biomed. Spectrosc. Imaging*, 2017, **6**, 59.
59 M. Hammad, W. Rao, J. G. W. Smith, D. G. Anderson, R. Langer, L. E. Young, D. A. Barrett, M. C. Davies, C. Denning and M. R. Alexander, *Biomater. Sci.*, 2016, **4**, 1381.
60 Y. Ishihama, Y. Oda, T. Tabata, T. Sato, T. Nagasu, J. Rappsilber and M. Mann, *Mol. Cell. Proteomics*, 2005, **4**, 1265.
61 J. Crowe, A. Aubareda, K. McNamee, P. M. Przybycien, X. Lu, R. O. Williams, G. Bou-Gharios, J. Saklatvala and J. L. E. Dean, *PLoS One*, 2013, **8**, e77383.
62 L. S. Coelho-Rato, S. Parvanian, M. K. Modi and J. E. Eriksson, *Trends Cell Biol.*, 2024, **34**, 239.
63 S. Parvanian, F. Yan, D. Su, L. S. Coelho-Rato, A. P. Venu, P. Yang, X. Zou, Y. Jiu, H. Chen, J. E. Eriksson and F. Cheng, *Cytoskeleton*, 2020, **77**, 399.
64 B. Eckes, E. Colucci-Guyon, H. Smola, S. Nodder, C. Babinet, T. Krieg and P. Martin, *J. Cell Sci.*, 2000, **113**, 2455.
65 R. Bucki, D. V. Iwamoto, X. Shi, K. E. Kerr, F. J. Byfield, Ł. Suprewicz, K. Skłodowski, J. Sutaria, P. Misiak, A. Z. Wilczewska, S. Ramachandran, A. Wolfe, M. T. H. Thanh, E. Whalen, A. E. Patteson and P. A. Janmey, *J. Biol. Chem.*, 2023, **299**(8), 104963.
66 C. J. Flaim, S. Chien and S. N. Bhatia, *Nat. Methods*, 2005, **2**, 119.
67 G. Leoni, P. A. Neumann, N. Kamaly, M. Quiros, H. Nishio, H. R. Jones, R. Sumagin, R. S. Hilgarth, A. Alam, G. Fredman, I. Argyris, E. Rijcken, D. Kusters, C. Reutelingsperger, M. Perretti, C. A. Parkos, O. C. Farokhzad, A. S. Neish and A. Nusrat, *J. Clin. Invest.*, 2015, **125**, 1215.
68 K. I. Rathore, B. J. Kerr, A. Redensek, R. López-Vales, Y. J. Suh, P. Ponka and S. David, *J. Neurosci.*, 2008, **28**, 12736.
69 H. Sinno, M. Malholtra, J. Lutfy, B. Jardin, S. Winocour, F. Brimo, L. Beckman, K. Watters, A. Philip, B. Williams and S. Prakash, *J. Dermatol. Treat.*, 2013, **24**, 141.

70 P. M. Steinert, E. Candi, E. Tarcsa, L. N. Marekov, M. Sette, M. Paci, B. Ciani, P. Guerrieri and G. Melino, *Cell Death Differ.*, 1999, **6**(9), 916.
71 M. Klaas, K. Mäemets-Allas, E. Heinmäe, H. Lagus, T. Arak, M. Eller, K. Kingo, E. Kankuri and V. Jaks, *Cell. Mol. Life Sci.*, 2022, **79**, 1.
72 D. Singh, V. Rai and D. K. Agrawal, *Cardiol. Cardiovasc. Med.*, 2023, **7**, 5.
73 L. D. Kirkpatrick, J. W. Shupp, R. D. Smith, A. Alkhalil, L. T. Moffatt and B. C. Carney, *Wound Repair Regener.*, 2021, **29**, 117.
74 A. Kljuic, H. Bazzi, J. P. Sundberg, A. Martinez-Mir, R. O'Shaughnessy, M. G. Mahoney, M. Levy, X. Montagutelli, W. Ahmad, V. M. Aita, D. Gordon, J. Uitto, D. Whiting, J. Ott, S. Fischer, T. C. Gilliam, C. A. B. Jahoda, R. J. Morris, A. A. Panteleyev, V. T. Nguyen and A. M. Christiano, *Cell*, 2003, **113**, 249.
75 T. Moreno-Sosa, M. B. Sánchez, E. O. Pietrobon, J. M. Fernandez-Muñoz, F. C. M. Zoppino, F. J. Neira, M. J. Germanó, D. E. Cargnelutti, A. C. Innocenti, G. A. Jahn, S. R. Valdez and J. P. Mackern-Oberti, *Front. Immunol.*, 2021, **12**, 625617.
76 C. Li, Y. Xiong, Z. Fu, Y. Ji, J. Yan, Y. Kong, Y. Peng, Z. Ru, Y. Huang, Y. Li, Y. Yang, L. He, J. Tang, Y. Wang and X. Yang, *Cell. Mol. Biol. Lett.*, 2024, **29**, 1.
77 Y.-T. Wu, Z.-Q. Ru, Y. Peng, Z. Fu, Q.-Y. Jia, Z.-J. Kang, Y.-S. Li, Y.-B. Huang, S.-G. Yin, K. Guo, N.-X. Liu, C.-A. Feng, J. Tang, B.-Y. Zhang, Z. Yang, Y. Wang, X.-W. Yang, Y.-T. Wu, Z.-Q. Ru, Y. Peng, Z. Fu, Q.-Y. Jia, Z.-J. Kang, Y.-S. Li, Y.-B. Huang, S.-G. Yin, K. Guo, N.-X. Liu, C.-A. Feng, J. Tang, B.-Y. Zhang, Z. Yang, Y. Wang and X.-W. Yang, *Zool. Res.*, 2024, **45**(6), 1287–1299.
78 Q. Jia, Z. Fu, Y. Li, Z. Kang, Y. Wu, Z. Ru, Y. Peng, Y. Huang, Y. Luo, W. Li, Y. Hu, X. Sun, J. Wang, Z. Deng, C. Wu, Y. Wang and X. Yang, *ACS Appl. Mater. Interfaces*, 2024, **16**, 13422.
79 P. L. Else, *Prog. Lipid Res.*, 2020, **77**, 101017.
80 M. K. Edney, A. M. Kotowska, M. Spanu, G. F. Trindade, E. Wilmot, J. Reid, J. Barker, J. W. Aylott, A. G. Shard, M. R. Alexander, C. E. Snape and D. J. Scurr, *Anal. Chem.*, 2022, **94**, 4703.
81 Y. Liu, Z. Li, W. Li, X. Chen, L. Yang, S. Lu, S. Zhou, M. Li, W. Xiong, X. Zhang, Y. Liu and J. Zhou, *Int. Immunopharmacol.*, 2024, **126**, 111283.
82 B. S. Shea and A. M. Tager, *Open Rheumatol. J.*, 2012, **6**, 8.
83 M. Aoki, H. Aoki, P. Mukhopadhyay, T. Tsuge, H. Yamamoto, N. M. Matsumoto, E. Toyohara, Y. Okubo, R. Ogawa and K. Takabe, *Int. J. Mol. Sci.*, 2019, **20**, 3381.
84 A. Latif, L. E. Fisher, A. A. Dundas, V. Cuzzucoli Crucitti, Z. Imir, K. Lawler, F. Pappalardo, B. W. Muir, R. Wildman, D. J. Irvine, M. R. Alexander and A. M. Ghaemmaghami, *Adv. Mater.*, 2022, 2208364.
85 A. A. Dundas, S. Kern, V. Cuzzucoli Crucitti, D. J. Scurr, R. Wildman, D. J. Irvine and M. R. Alexander, *Surf. Interface Anal.*, 2022, **54**, 374.